

MATERIALS SCIENCE

Drift-dominant exciton funneling and trion conversion in 2D semiconductors on the nanogap

Hyeongwoo Lee^{1†}, Yeonjeong Koo^{1†}, Jinseong Choi¹, Shailabh Kumar², Hyoung-Taek Lee¹, Gangseon Ji¹, Soo Ho Choi³, Mingu Kang¹, Ki Kang Kim^{3,4}, Hyeong-Ryeol Park¹, Hyuck Choo^{2,5}, Kyoung-Duck Park^{1*}

Understanding and controlling the nanoscale transport of excitonic quasiparticles in atomically thin two-dimensional (2D) semiconductors are crucial to produce highly efficient nano-excitonic devices. Here, we present a nanogap device to selectively confine excitons or trions of 2D transition metal dichalcogenides at the nanoscale, facilitated by the drift-dominant exciton funneling into the strain-induced local spot. We investigate the spatio-spectral characteristics of the funneled excitons in a WSe₂ monolayer (ML) and converted trions in a MoS₂ ML using hyperspectral tip-enhanced photoluminescence imaging with <15-nm spatial resolution. In addition, we dynamically control the exciton funneling and trion conversion rate by the gigapascal-scale tip pressure engineering. Through a drift-diffusion model, we confirm an exciton funneling efficiency of ~25% with a significantly low strain threshold (~0.1%), which sufficiently exceeds the efficiency of ~3% in previous studies. This work provides a previously unexplored strategy to facilitate efficient exciton transport and trion conversion of 2D semiconductor devices.

INTRODUCTION

A distinguished advantage of atomically thin semiconductors compared to other types of low-dimensional quantum materials, such as zero-dimensional (0D) quantum dots and 1D nanowires, is the wide exciton distribution over a 2D area. On the one hand, this fascinating property provides substantial benefits to fabricate highly efficient and ultrathin optoelectronic devices operating at room temperature, especially in photovoltaics (1) and light-emitting devices (2). On the other hand, to exploit excitons as carriers for quantum information devices and exciton-integrated circuits, e.g., using single-photon-emitting localized excitons (3) or long-coherence dark excitons (4) as well as neutral and charged excitons (5, 6), controlling the exciton dynamics is a challenging subject. To manipulate the exciton dynamics of 2D transition metal dichalcogenides (TMDs), e.g., drift-induced excitonic flux and diffusion-induced energy conversion, various strain-engineering approaches have been demonstrated recently (5, 6). The electronic band structure and excitonic properties of 2D semiconductors can be significantly modified by tuning the crystal strain owing to their atomic thickness. Hence, many studies attempted to achieve the deterministic exciton funneling to a low bandgap region by fabricating strain-gradient devices, e.g., using wrinkled substrates (7), piezoelectric actuators (8), and atomic force microscopy (AFM) tips (5, 6). However, recent works revealed that the exciton funneling efficiency using these approaches is significantly low (<3%) at room temperature because of the dominant diffusion in the microscale bandgap-gradient regions overwhelming the required drift process (6, 9). Specifically, because the drift process has a directionality in the bandgap-gradient region in contrast to the random-directional

diffusion process, increasing the ratio of the drift-dominant region is a crucial factor to achieve the high funneling efficiency. Up to present, most studies induced a massive strain on the crystal, deteriorating the crystal quality and radiative quantum yield (7). Therefore, designing an ideal TMD device, e.g., with high exciton funneling efficiency and large quantum yield with an insignificant induced strain, is highly desirable. In addition, to raise the degree of integration of quantum devices and exciton-integrated circuits, the exciton funneling channel must be significantly scaled down compared to the current microscale dimensions.

Another intriguing observation in the previous study was the trion conversion at the funneling region in a WS₂ monolayer (ML) (6). In particular, they found that the free carriers are efficiently funneled into the lowest bandgap region and coupled to neutral excitons (X₀) to form the trion (X⁻) state with almost 100% conversion efficiency without electrical gating even at room temperature. This remarkable property can widely expand the scope of applications in 2D excitonic devices with the ability to control the dynamics of excitons and trions. However, because the previous work only investigated the exciton funneling and trion conversion of n-type TMD MLs with a microscale strain gradient with diffraction-limited far-field spectroscopy, it introduced confusion with the role of doping types and the size of the bandgap-gradient region. Hence, a high-resolution spatio-spectral investigation for various TMD MLs with a correlated analysis of the structural, optical, and theoretical properties is crucial to understand the exciton dynamics at its natural length scale comprehensively.

Here, we present a nanogap device to facilitate the low-threshold and highly efficient exciton funneling and trion conversion processes even at room temperature. The nanoscale strain-gradient region induced by the nanogap enables the drift-dominant region to occupy more than ~60% of the strain-gradient area. It leads to the high exciton funneling efficiency exceeding ~25% estimated by a drift-diffusion model designing the WSe₂ and MoS₂ MLs on the nanogap (6). To experimentally confirm these nanoscale exciton funneling and trion conversion, we use hyperspectral tip-enhanced photoluminescence (TEPL) imaging with a spatial resolution of ~15 nm

¹Department of Physics, Ulsan National Institute of Science and Technology (UNIST), Ulsan 44919, Republic of Korea. ²Department of Medical Engineering, California Institute of Technology (Caltech), Pasadena, CA 91125, USA. ³Center for Integrated Nanostructure Physics, Institute for Basic Science (IBS), Suwon 16419, Republic of Korea. ⁴Department of Energy Science, Sungkyunkwan University (SKKU), Suwon 16419, Republic of Korea. ⁵Imaging Device Lab, Device and System Research Center, Samsung Advanced Institute of Technology (SAIT), Suwon 16678, Republic of Korea.

*Corresponding author. Email: kdpark@unist.ac.kr

†These authors contributed equally to this work.

(see fig. S1 for details). It reveals that the observed PL enhancement of $\sim 180\%$ with $\sim 0.1\%$ strain is comparable to the PL enhancement from the microscale strain gradient achieved with more than $\sim 10\%$ strain for a WSe_2 ML (7). For a MoS_2 ML, in contrast, exciton-to-trion conversion is observed at the nanogap region. In addition, we use the plasmonic tip for the nano-opto-mechanical control of these TMD crystals. By directly pressing and releasing the crystal with gigapascal-scale tip pressure, we dynamically engineer ~ 10 times greater strain on the TMD crystal at the nanoscale. This experiment demonstrates the ability to gradually tune the exciton funneling and trion conversion rates in TMD MLs in a reversible manner.

RESULTS

Precharacterizations of TMD MLs on the nanogap

To facilitate an efficient exciton funneling and trion conversion for WSe_2 and MoS_2 MLs and to further investigate their spatial dynamics in the subwavelength-scale region, we use the nanogap device combined with TEPL spectroscopy, as illustrated in Fig. 1A. The WSe_2 and MoS_2 MLs are transferred onto the nanogap device with a gap size of ~ 150 to 300 nm to induce a nanoscale strain gradient to the ML crystals at the nanogap region (see Materials and Methods for more details). When the excitation beam (632.8 nm) is focused to the TMD MLs on the nanogap, the photoexcited excitons are generated and drifted toward the nanogap center, i.e., the lowest potential energy region, attributed to the strain-gradient effect. Figure 1 (B and C) shows energy diagrams of the WSe_2 and MoS_2 MLs on the nanogap, describing the distinguished dynamics of electric charges and excitons under the same strain-gradient condition. The largest strain induced at the gap center gives rise to the smallest bandgap for both WSe_2 and MoS_2 MLs, which stimulates the funneling of excitons and electrons toward it. In the WSe_2 ML, only neutral excitons are dominantly funneled toward the gap because it has few electrons. In contrast, in the MoS_2 ML, electrons are dominantly drifted to the gap apart from the exciton funneling (6) because it is a naturally n-type doped material (10). In addition, the funneled

excitons are converted to the trion state by the overflowing electrons in the gap. We use TEPL spectroscopy to characterize these exciton dynamics and trion conversion in their natural physical length scale, as shown in Fig. 1A. Note that we maintain a ~ 10 -nm tip-sample distance to avoid the possible perturbation effect to the crystal by the Au tip.

In addition to probing exciton and trion properties, this approach controls these dynamics at the nanoscale. Specifically, in our home-built TEPL setup, the electrochemically etched Au tip (apex radius of ~ 15 nm) enhances the PL signal and gives a spatial resolution of ~ 15 nm by the nano-optical antenna effect and Purcell enhancement (3, 11). Furthermore, our shear-force AFM module offers a nanoscale 3D positioning of the Au tip with <0.2 -nm precision, facilitating a systematic strain engineering and exciton/trion control of the WSe_2 and MoS_2 MLs with measuring of TEPL signals simultaneously (see Materials and Methods for more details). The well-suspended TMD ML on the nanogap to generate the strain-gradient effect is precharacterized through AFM measurements, as shown in Fig. 1 (D and E). Topography images of the nanogap with and without the MoS_2 ML exhibit a difference in depth, as indicated by the topographic line profiles in Fig. 1E.

Exciton dynamics and trion conversions in nanoscale wrinkles

The ideal nanoscale strain-gradient structure for effective X_0 funneling and X- conversion exists in nature, i.e., the nanoscale wrinkle in 2D TMDs. Our previous study revealed the exciton funneling behaviors of the naturally formed wrinkles in a WSe_2 ML (12). As experimentally confirmed again in this study, the uniaxial tensile strain is induced in the wrinkle structure with the highest strain at the apex region, which facilitates the exciton funneling to the lowest bandgap energy region, spatially at the nanoscale. Figure 2A shows the TEPL spectra of a WSe_2 ML when the Au tip is placed at the crystal face and the wrinkle. The peak red shift of ~ 3 meV at the wrinkle compared to the peak energy at the crystal face allows us to estimate the induced tensile strain of $\sim 0.05\%$ at the wrinkle apex

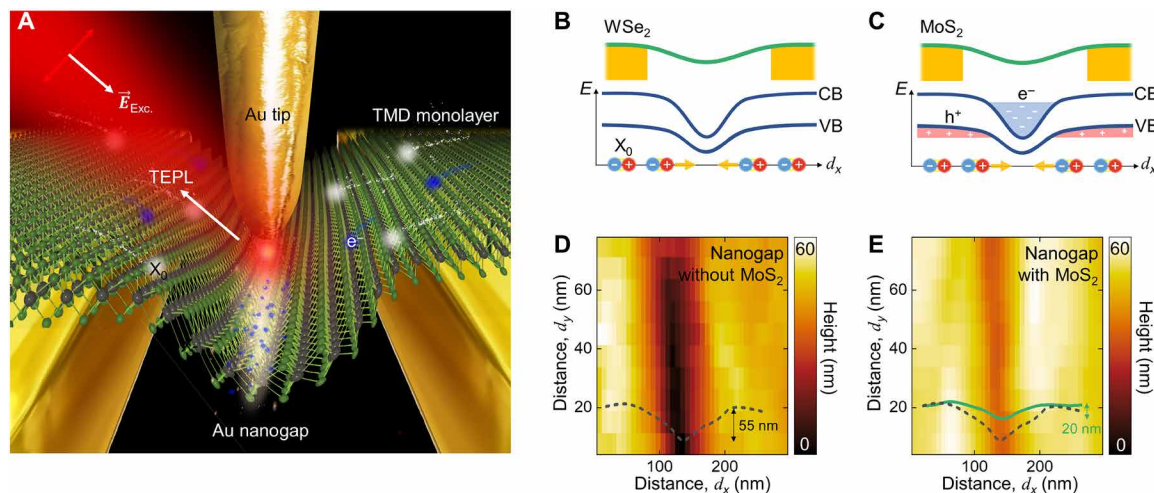


Fig. 1. Schematic illustrations of an experimental design and energy diagram. (A) The Au nanogap device and transferred TMD MLs combined with TEPL spectroscopy to probe and control the electric charges (e^-) and exciton (X_0) dynamics at the nanoscale. Illustrations of the energy band diagram for WSe_2 (B) and MoS_2 , CB, conduction band; VB, valence band. (C) MLs on the nanogap and spatial distributions of electric charges (e^- and h^+) and photoexcited excitons (X_0). AFM topography images and height profiles of the nanogap without (D) and with (E) MoS_2 ML exhibiting a wrinkled crystal structure, which gives rise to a nanoscale strain gradient.

(13). The TEPL intensity at the wrinkle increases by $\sim 140\%$ compared to the TEPL intensity at the crystal face by the exciton funneling effect. This increased PL ratio is comparable to the previous study obtained by inducing a significantly higher strain of $\sim 5\%$ with the microscale strain-engineering technique (7). That is a markedly improved exciton funneling efficiency with respect to the induced strain that is obtained at this nanoscale strain-gradient structure (wrinkle). The specific details for the physical mechanism are depicted with a theoretical model in the later part, which was not considered in our recent report (12). In contrast, the TEPL intensity decreases with distinctly increased linewidth at the wrinkle for a MoS₂ ML compared to the crystal face region, as shown in Fig. 2B. This inverse feature at the wrinkle between WSe₂ and MoS₂ MLs is attributed to the doping type of TMD crystals. Therefore, the electron funneling along with a trion conversion is the dominant process at the wrinkle for the n-type doped MoS₂ ML. We will discuss the spatial dynamics of excitons and electric charges, and the trion conversion, for different TMDs in the nanoscale strain-gradient structures after demonstrating the results of our control experiments first.

To investigate the efficient exciton funneling in a WSe₂ ML and the trion conversion in a MoS₂ ML, we obtain hyperspectral TEPL images at the wrinkles (Fig. 2, C to J). As expected from the TEPL point spectra in Fig. 2A, a large TEPL signal at the wrinkle apex is observed in the integrated intensity image for neutral excitons (I_{X_0} , 1.663 to 1.703 eV; Fig. 2, C and D) for a WSe₂ ML. We also observe the marginally increased integrated intensity for trions (I_{X^-} , 1.593 to 1.633 eV; Fig. 2E) with the broadened linewidth (Fig. 2F). However, the significant modifications are not observed compared to the X_0 emission. On the contrary, the TEPL intensity for neutral excitons (I_{X_0} , 1.902 to 1.942 eV) shows a pronounced decrease at the wrinkle for a MoS₂ ML, as shown in Fig. 2 (G and H). Furthermore, we observe the distinct increase of the integrated intensity for trions (I_{X^-} ,

1.832 to 1.872 eV; Fig. 2I) with the significantly broadened linewidth (Fig. 2J) at the wrinkle apex because of the efficient trion conversion.

Deterministic exciton funneling and trion conversion using nanogap

Nanoscale wrinkles are attractive nanostructures for efficient exciton funneling and trion conversion. However, their applications to exciton-integrated circuits or other excitonic devices are restricted because of their random locations. Hence, to deterministically control the exciton energy and spatial dynamics at the nanoscale, we fabricate the strain gradient of WSe₂ and MoS₂ MLs by the nanogap, i.e., the inverse-wrinkle structure at a specific location. Figure 3A shows a TEPL spectrum of a WSe₂ ML at the nanogap, exhibiting an intensity increase with slight peak red shift (red), compared to the TEPL spectrum measured at the Au surface (green). The peak red shift is attributed to the bandgap bending induced by a uniaxial tensile strain of $\sim 0.1\%$ (13), which is followed by the exciton funneling and consequent TEPL intensity increase of $\sim 180\%$. These features are similar to the results of a WSe₂ wrinkle (Fig. 2A). In contrast, Fig. 3B shows an asymmetric TEPL spectrum of a MoS₂ ML on the Au surface by the existence of trions (green). The asymmetry of a TEPL spectrum measured at the nanogap becomes significantly apparent with decreased emission intensity. This different spectral feature between the WSe₂ and MoS₂ crystals originated from the excess electrons in the MoS₂ ML. Because MoS₂ is an electron-rich TMD crystal, the distinguishable X⁻ shoulder is naturally observed in the flat crystal even at room temperature (10, 14). The X⁻ peak becomes more significant with the local strain gradient because the electrons are funneled to the lower-bandgap energy region together with neutral excitons, and they are converted to trions (6). The decreased X_0 TEPL intensity with the emerging X⁻ peak at the nanogap center well supports this trion conversion process.

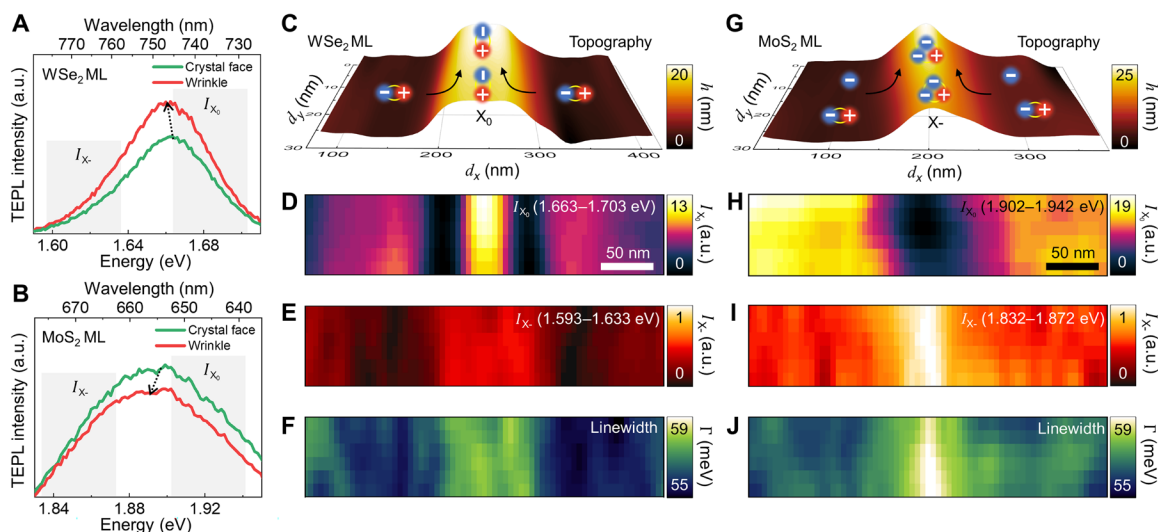


Fig. 2. Hyperspectral TEPL imaging of strained TMD MLs at the wrinkle. TEPL spectra of WSe₂ (A) and MoS₂ (B) MLs at the crystal face (green) and the wrinkle (red) regions. (C to F) Hyperspectral TEPL images of a WSe₂ ML. AFM topography image with a description of exciton funneling (C). TEPL images of the spectrally integrated intensity of excitons (D) [spectral region of I_{X_0} in (A)] and low-energy shoulder (E) [spectral region of I_{X^-} in (A) after normalization]. TEPL image of spectral linewidth (F). (G to J) Hyperspectral TEPL images of a MoS₂ ML. AFM topography image with a description of electron funneling and trion (X⁻) conversion (G). TEPL images of the spectrally integrated intensity of excitons (H) [spectral region of I_{X_0} in (B)] and low-energy shoulder (I) [spectral region of I_{X^-} in (B) after normalization]. TEPL image of spectral linewidth (J). a.u., arbitrary units.

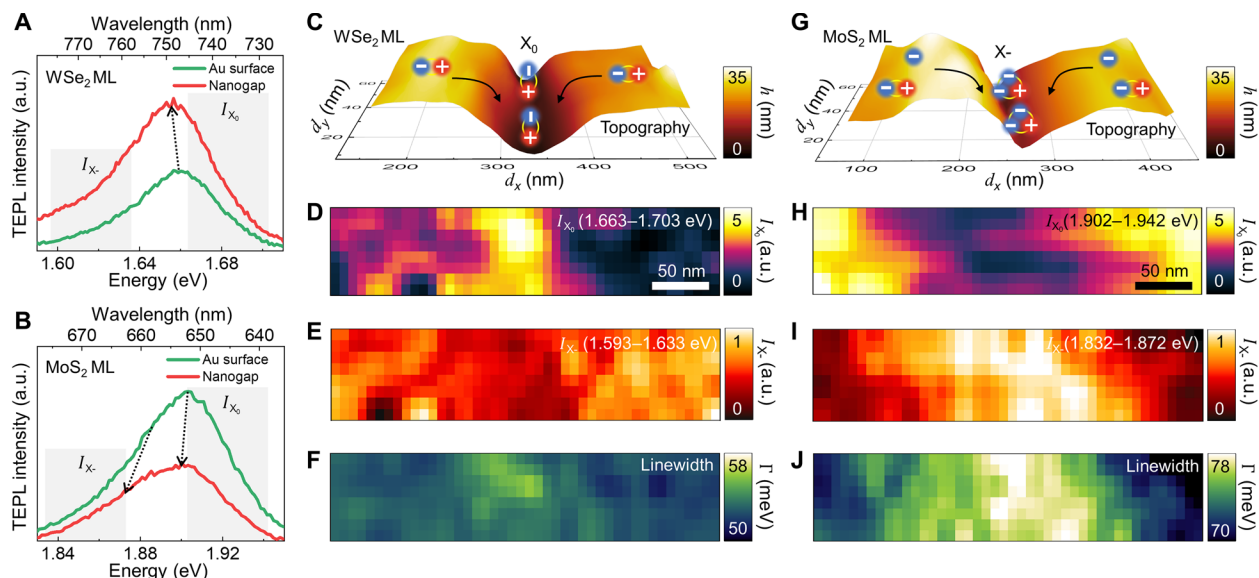


Fig. 3. Hyperspectral TEPL imaging of TMD MLs at the nanogap. TEPL spectra of WSe₂ (A) and MoS₂ (B) MLs at the Au surface (green) and the nanogap (red) regions. (C to F) Hyperspectral TEPL images of a WSe₂ ML. AFM topography image with a description of exciton funneling (C). TEPL images of the spectrally integrated intensity of excitons (D) [spectral region of I_{X_0} in (A)] and low-energy shoulder (E) [spectral region of I_X in (A) after normalization]. TEPL image of spectral linewidth (F). (G to J) Hyperspectral TEPL images of a MoS₂ ML. AFM topography image with a description of electron funneling and trion (X^-) conversion (G). TEPL images of the spectrally integrated intensity of excitons (H) [spectral region of I_{X_0} in (B)] and low-energy shoulder (I) [spectral region of I_X in (B) after normalization]. TEPL image of spectral linewidth (J).

To more clearly investigate their exciton funneling and trion conversion processes, we perform hyperspectral TEPL imaging. Figure 3 (C to F) shows the measured AFM topography, integrated TEPL intensity images of neutral excitons (I_{X_0} , 1.663 to 1.703 eV) and trions (I_X , 1.593 to 1.633 eV), and TEPL linewidth map of a WSe₂ ML. We observe the expected spatial dynamics of excitons moving into the topographical valley, i.e., exciton drifts toward the strain-maximum region. In contrast, the spatial maps of trion TEPL intensity and TEPL linewidth show no significant differences at the nanogap compared to the Au surface region. The MoS₂ ML on the nanogap shows different behaviors for neutral excitons (I_{X_0} , 1.902 to 1.942 eV) and trions (I_X , 1.832 to 1.872 eV), as shown in Fig. 3 (G to J). Because the drifted neutral excitons and electrons are expected to be converted to trions, I_{X_0} decreases at the nanogap (Fig. 3H). Meanwhile, the I_X shows a considerable increase at the nanogap (Fig. 3I), and the converted trion peak gives rise to the linewidth increase (Fig. 3J). Our artificially fabricated strain-gradient TMDs at the nanogap generally show similar characteristics to the naturally formed nanoscale wrinkles in WSe₂ and MoS₂ MLs. Therefore, we confirm the on-demand capability of deterministic exciton funneling and trion conversion at the nanoscale with high efficiency.

Dynamic control of exciton funneling and trion conversion via gigapascal tip pressure

We investigate the detailed trion conversion process of a MoS₂ ML at the nanoscale strain gradient by measuring the evolution of TEPL spectra when the Au tip laterally moves toward the nanogap center (Fig. 4A). As shown in Fig. 4B, the gradual red shift of X_0 peak represents the formation of a strain gradient of a MoS₂ ML, which has a maximum strain of $\sim 0.1\%$ at the center (15). In addition, the X^- shoulder emerges, and its intensity increases as the induced strain increases. To better represent the spectral changes with respect to the increased strain, we normalize the series of TEPL spectra and

subtract the TEPL spectrum measured at the Au surface from them, as shown in Fig. 4C. The X^- peak evolution from the edge to the nanogap center is observed in the subtracted TEPL spectra. The detailed discussion for the contribution of the neutral exciton density to the trion density is presented in figs. S2 and fig. S3.

We then demonstrate dynamic control of exciton funneling and trion conversion by directly pressing and releasing the crystal with the Au tip. In our numerical simulations (Fig. 4D), the strain-gradient maximum shows the gradual increase as the Au tip presses a TMD ML at the nanogap center. Accordingly, we can derive the applied pressure and the strain on a TMD ML as a function of the applied force by the Au tip, as shown in Fig. 4E. This result shows that the key feature of our approach is the control of extremely large pressure at the gigapascal scale with the \sim piconewton-scale force because the unit area of the Au tip is on the order of 10^2 nm^2 . In addition, we can simultaneously measure TEPL responses with a spatial resolution of $\sim 15 \text{ nm}$ and dynamically engineer the tip-induced strain on the crystal, which was not allowed in other works (16). Figure 4 (F and G) shows the experimental results of the tip-induced strain control and corresponding modification of TEPL spectra for WSe₂ and MoS₂ MLs. When the Au tip presses the WSe₂ ML, X_0 TEPL intensity increases with the increasing exciton funneling rate, whereas it decreases to the original state when the tip releases from the crystal. In contrast, X_0 TEPL intensity decreases as the Au tip presses the MoS₂ ML with the increasing trion conversion rate, whereas it returns to the original state as the tip releases. The detailed analysis on these reversible TEPL intensity changes of X_0 and X^- is presented in fig. S4.

Theoretical investigations of nanoscale exciton transport

To quantitatively understand the advantages of the nanoscale strain gradient compared to the previously studied microscale strain-gradient geometry (5–7), we perform numerical analysis on TMD MLs under

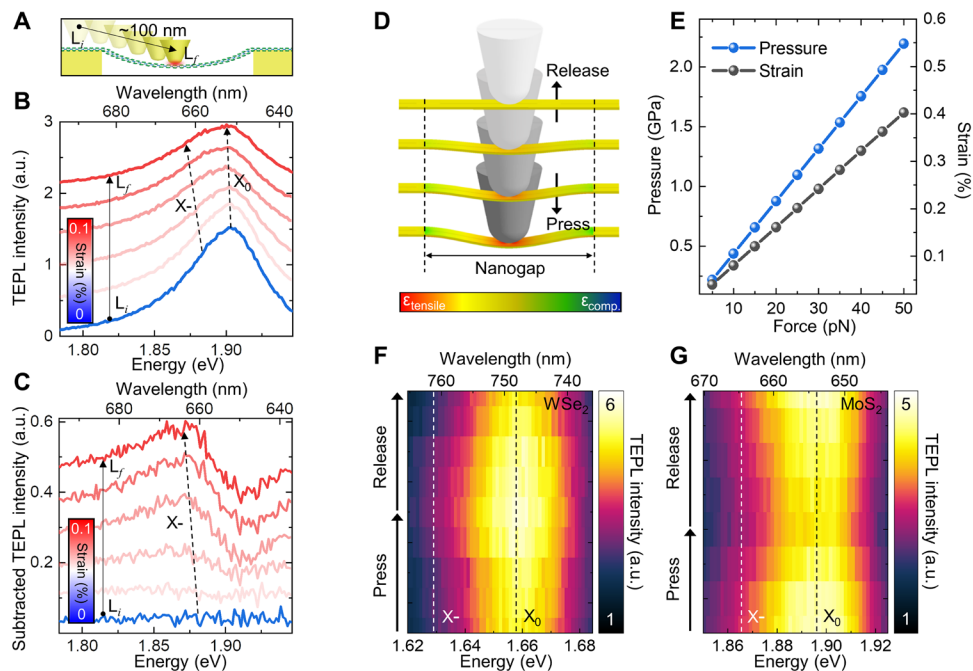


Fig. 4. Tip-induced control of exciton funneling and trion conversion. (A) Schematic illustration for the lateral tip movement from L_i to L_f (distance of ~ 100 nm). (B) TEPL spectra of a MoS_2 ML at the nanogap when the Au tip moves from L_i to L_f . (C) Subtracted TEPL spectra exhibiting the pronounced spectral modification. To obtain these results, all the spectra in (B) are normalized and subtracted by the spectrum at 0% strain [blue in (B)]. (D) Simulated strain distribution for TMD MLs on the nanogap as the Au tip presses and releases the crystal. (E) Calculated local pressure and strain of the crystal as a function of the force applied by the Au tip. (F and G) Reversibly engineered TEPL spectra of WSe_2 (F) and MoS_2 (G) MLs by the tip force, exhibiting nanoscale dynamics of excitons and trions. Black and white dashed lines indicate the energy of neutral excitons (X_0) and trions (X^-).

the strain gradient. First, we model a strain-gradient profile on the basis of the experimentally obtained strain distribution at the nanogap, as shown in Fig. 5A (see fig. S5 for more details) (15). We then analyze the drift-diffusion equation of MoS_2 and WSe_2 MLs with the modeled strain-gradient profile (6, 17). The experimental values of the Auger recombination rate, exciton lifetime, and diffusion coefficient of WSe_2 and MoS_2 MLs for solving the equation are derived from previous studies (18–20). Figure 5B shows the exciton density distributions of a MoS_2 ML at the ~ 3 - μm microgap and the ~ 300 -nm nanogap under the same applied strain of $\sim 0.1\%$. To investigate the contribution of the exciton drift to the spatial distribution, we subtract the exciton density without strain gradient $n_0(x)$ from the exciton density with strain gradient $n_{\text{gap}}(x)$ (see fig. S6 for more details). For both microgap and nanogap, the exciton density increases at the center of the gap, whereas it decreases in the vicinity, representing the exciton funneling phenomenon. However, the concentration of the drifted exciton at the center is much weaker and broader at the microgap compared to the nanogap. To quantitatively estimate the exciton funneling efficiency of the microgap and nanogap to the ~ 15 -nm tip apex region, we define the following equation

$$\text{Funneling efficiency, } \eta = \frac{\int_0^{x_{\text{tip}}} \{n_{\text{gap}}(x) - n_0(x)\} dx}{\int_0^{x_{\text{gap}}} \{n_{\text{gap}}(x) - n_0(x)\} dx} \quad (1)$$

We obtain $\eta \approx 25$ and 0.8% for the nano- and microgaps, respectively (see calculation of the funneling efficiency in the Supplementary Materials for more details). Note that we exclude the existence of the electron in this step to precisely investigate the exciton funneling efficiency.

We can understand the markedly enhanced funneling efficiency at the nanogap by comparing the portion of drift-dominant region in the microscale and nanoscale strain gradients. In the drift-diffusion model, the drift-dominant region with respect to the temperature T is given by

$$k_B T < \frac{S(x) \nabla u(x)}{\nabla S(x)} \quad (2)$$

where k_B , $S(x)$, and $u(x)$ are the Boltzmann constant, exciton generation rate under the Gaussian beam profile, and strain profile, respectively. It indicates that the drift dominates over the diffusion when the right-hand term is larger than the thermal energy of ~ 25 meV at room temperature (6). Figure 5C shows the drift-dominant region of ~ 100 nm, which occupies more than $\sim 60\%$ of a whole strain-gradient region. Hence, we achieve higher funneling efficiency even with significantly smaller strain $\varepsilon \approx 0.1\%$ compared to the microscale strain-gradient geometry to facilitate the low-threshold exciton transport, i.e., to achieve high-efficiency exciton funneling with low strain threshold. The increased exciton intensity with $\varepsilon \approx 0.1\%$ in Fig. 3A is comparable to the microscale strain-gradient geometry with $\varepsilon \approx 10\%$ (7). If we define a parameter α indicating a ratio between the funneling efficiency and strain as

$$\alpha = \frac{\eta}{\varepsilon} \quad (3)$$

then the expected value is $\alpha \approx 250$ for a WSe_2 ML on the nanogap ($\eta \approx 25\%$, $\varepsilon \approx 0.1\%$), which significantly exceeds $\alpha \approx 1$ of the previous study (6).

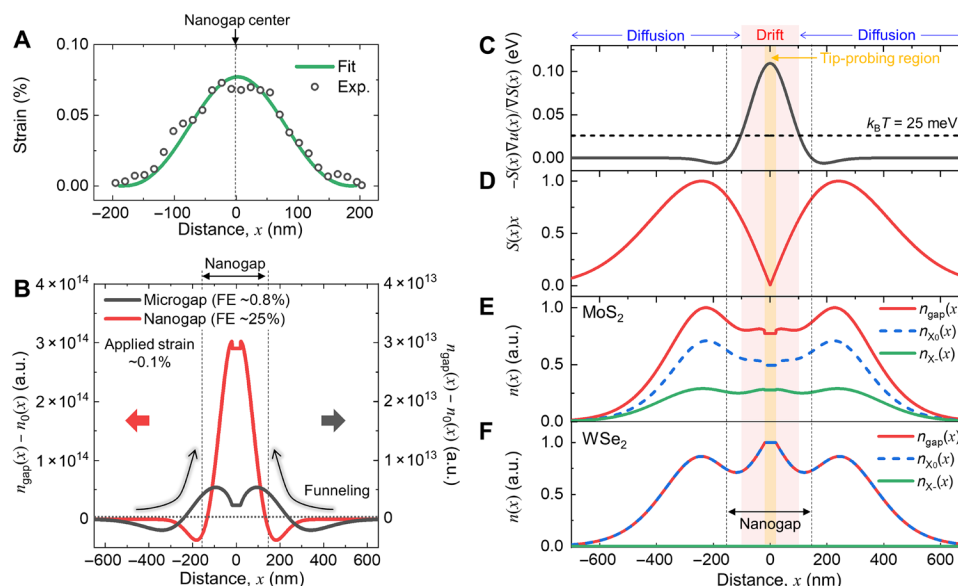


Fig. 5. Spatial distribution of excitons and trions at the nanogap. (A) Strain distribution of a MoS₂ ML on the nanogap obtained from the exciton TEPL peak energy shift (black dots) and fitted line shape function (green line). (B) Spatial density distribution of neutral excitons at the microgap (black) and the nanogap (red) for a MoS₂ ML under the applied strain of ~0.1%. $n_{\text{gap}}(x)$ and $n_0(x)$ indicate their spatial density with and without the gap, respectively. FE, funneling efficiency. (C) Spatial distribution of the ratio between the drift and diffusion terms $[-\frac{S(x)\nabla u(x)}{\nabla S(x)}$, solid line) and thermal energy $k_B T$ at room temperature (dashed line). The drift-dominant (shaded) and diffusion-dominant regions are classified. The yellow shaded region indicates the tip-probing region in TEPL measurements. (D) Spatial distribution of the optical source term $S(x)x$ in our experiment. (E and F) Normalized density distribution of neutral excitons $n_{X0}(x)$ and trions $n_X(x)$ at the nanogap for MoS₂ (E) and WSe₂ (F) MLs.

The distribution of photoexcited excitons follows the illumination spot considering the area factor, as shown in Fig. 5D. The exciton density distribution is significantly modified by the strain gradient because of the exciton funneling effect. In addition, to include the trion conversion effect by the nanogap, we estimate the electron density as a function of the distance on the basis of the Boltzmann distribution as follows

$$n_e(x) = \frac{N_0 e^{\nabla u_c(x)/k_B T}}{\int e^{\nabla u_c(x)/k_B T} dx} \quad (4)$$

where N_0 is the number of free carriers in the nanogap and $\nabla u_c(x)$ is the change of energy of the conduction band (6). From the estimated $n_e(x)$, we obtain the distributions of exciton density and trion density for MoS₂ and WSe₂ MLs in our experimental condition, as shown in Fig. 5 (E and F) (see figs. S6 and S8 for more details). Note that $n_{\text{gap}}(x)$ is a summation of $n_{X0}(x)$ and $n_X(x)$. In the simulated results, the formation of trion with decreased number of neutral exciton by the trion conversion is observed for a MoS₂ ML. In contrast, only the increased number of neutral exciton is observed for a WSe₂ ML because $n_e(x) \approx 0$ for the p-doped WSe₂ ML (5).

DISCUSSION

Our work presents a low-threshold exciton transport and its dynamic control through the TMD on a nanogap platform combined with TEPL spectroscopy. We experimentally observe ~180% increase of TEPL intensity with ~0.1% strain at the nanogap, which is a comparable effect to the microscale strain gradient induced with ~10% strain. That is, our approach allows a significant decrease of the strain threshold for facilitating recognizable exciton funneling. This

result is attributed to the high funneling efficiency of the nanoscale strain gradient, which enables to occupy the drift-dominant region more than ~60% of the whole strain-gradient region. In addition, spatial positioning with ~0.2-nm precision and gigapascal-scale pressure of the Au tip leads to the dynamic control of exciton dynamics, e.g., control of exciton funneling rate in WSe₂ and trion conversion rate in MoS₂ in a reversible manner. The presented efficient spatial manipulation of exciton dynamics at the nanoscale is highly desirable for further advances of exciton-based optoelectronics. Thus, we envision that our approach will provide on-demand nanoscale positioning of the efficient strain-gradient platform, enabling higher quantum efficiency and a greater degree of integration for the next-generation exciton-based optoelectronic devices.

MATERIALS AND METHODS

Growth and transfer of WSe₂ MLs

To transfer commercially available chemical vapor deposition-grown WSe₂ ML onto a nanogap device, a wet transfer process was used. First, polymethyl methacrylate (PMMA) was spin-coated onto WSe₂ ML grown on the SiO₂ substrate. Then, the PMMA-coated WSe₂ ML was separated from the SiO₂ substrate using a hydrogen fluoride solution and carefully transferred onto the nanogap device after being rinsed in distilled water to remove residual etchant. Next, it is dried naturally for 6 hours to improve the adhesion. Last, the PMMA was removed using acetone.

Growth and transfer of MoS₂ MLs

A two-zone furnace was used to grow ML MoS₂ flakes. Sulfur flakes (Merck, ≥99.99%) were positioned in the upstream zone. As a molybdenum precursor, 0.01 M sodium molybdate aqueous solution

was spun onto the SiO₂/Si substrate. The substrate was loaded into the downstream zone. The sulfur flakes and the substrate were heated at 200° and 750°C temperatures for 7 min and maintained for 8 min. Then, the substrate was naturally cooled down to room temperature. The entire process was conducted under N₂ carrier gas with a flow rate of 600 sccm. Then, as-grown MoS₂ was coated with PMMA under 2500 rpm for 1 min. To delaminate the SiO₂/Si substrate, the PMMA-coated sample was floated on a 2 M KOH aqueous solution. After the delamination, underneath KOH residues were rinsed by deionized water several times. The PMMA/MoS₂ layer was scooped by the nanogap-patterned substrate. The PMMA layer was removed by acetone and isopropyl alcohol.

Fabrication of the nanogap by focused ion beam

Single-side-polished silicon wafers with thermally grown SiO₂ with a thickness of 1 μm were purchased from UniversityWafer, Boston, USA. Electron beam evaporation was used to deposit 50-nm gold on the wafers. FEI Nova 600 dual-beam system was used to perform focused ion beam milling on the wafers to remove the gold from the silica surface, creating the nanogap. This was performed at an ion beam voltage of 30 kV and a current of 1 pA.

Fabrication of the nanogap by atomic layer lithography

The rectangular-shaped nanogap was fabricated using atomic layer lithography technique (21). First, we performed a conventional photolithography with a negative photoresist of MA-N-1410 (Micro Resist Technology GmbH, Germany), which was spin-coated at 3000 rpm for 30 s onto a 500-μm-thick silicon substrate and then soft-baked at 100°C for 90 s. The sample was exposed to ultraviolet light (i-line, intensity of about 10 mW/cm²) for 40 s using a mask aligner (MA6, SÜSS MicroTec, Garching, Germany). After the sample was developed by ma-D-533/S developer, Cr/Au layers, with thickness of 5 and 100 nm, respectively, were deposited on patterned samples by an electron beam evaporator, and a subsequent liftoff process is performed with an *N*-methyl-2-pyrrolidone solution. A 20-nm-thick aluminum oxide (Al₂O₃), which determines the gap size, was deposited by atomic layer deposition (ALD) at 250°C. After the ALD process, an 80-nm-thick Au layer was deposited on a patterned sample to fill inside rectangular holes, and it formed a metal-insulator-metal structure. A simple adhesive tape-based peel-off process was performed to planarize the nanogap surface. Here, we used the Ar-ion miller (KVET-IM2000L, Korea Vacuum Tech, Gimpo, Korea) with an oblique angle of 85°, acceleration voltage of 80 V, beam current of 1.3 mA, and exposure time of 10 min to make the peel-off process easier. Then, the sample was immersed in buffered oxide etchant 6:1 solution (J.T.Baker, USA) for 20 s to remove the top side of the aluminum oxide layer (Al₂O₃). After these processes, the sample was exposed for 15 min under the oblique ion milling conditions same as the above to smoothen any difference in the heights of the first and second metal layers.

TEPL spectroscopy setup

The prepared TMD MLs on the nanogap were loaded on a piezoelectric transducer (P-611.3X, Physik Instrumente) for XY scanning and applying the dynamic pressure control with <0.2-nm positioning precision. To press and release suspended TMD MLs, a Au tip (apex radius of ~15 nm) was used. The Au tip, which was fabricated with a refined electrochemical etching protocol, was attached to a quartz tuning fork (resonance frequency of 32.768 kHz) to regulate

the distance between the tip and sample on the basis of shear-force AFM operated by a digital AFM controller (R9+, RHK Technology). For TEPL experiments, a conventional optical spectroscopy setup was combined with home-built shear-force AFM. For a high-quality wavefront of the excitation beam, a He–Ne laser (632.8 nm, <0.5 mW) was coupled and passed through a single-mode fiber (core diameter of ~3.5 μm) and collimated again using an aspheric lens. The collimated beam was then passed through a half-wave plate to make the excitation polarization parallel to the tip axis. Last, the beam was focused onto the Au tip using a microscope objective (numerical aperture = 0.8; LMPLFLN100X, Olympus) with a side illumination geometry. To ensure highly efficient laser coupling to the Au tip, the tip position was controlled with ~30-nm precision by Picomotor actuators (9062-XYZ-PPP-M, Newport). TEPL responses were collected using the same microscope objective (backscattering geometry) and passed through an edge filter (LP02-633RE-25, Semrock) to cut off the fundamental laser line. TEPL signals were then dispersed onto a spectrometer (*f* = 328 mm, Kymera 328i, Andor) and imaged with a thermoelectrically cooled charge-coupled device (iDus 420, Andor) to acquire TEPL spectra. Before the experiment, the spectrometer was calibrated with an argon mercury lamp. A grating of 150 g/mm blazed to 800 nm (spectral resolution of 0.62 nm) was used for PL measurements.

Simulation of the tip-induced local pressure, strain, force, and strain distribution

To quantify the tip-induced mechanical properties applied on the contact region between the Au tip and the TMD MLs, the experimental conditions were modeled and calculated using a commercially available 3D simulation program, the Mechanical Enterprise module from ANSYS. In the model, the material of the Au tip was set to gold in the program. The material properties of the TMD MLs, such as Young's modulus, the Poisson ratio, and density, were derived from Zhang *et al.* (22). The vertical position of the tip was located at the center of the nanogap structure before starting the simulation. Both ends of the TMD MLs were considered to be not slipped on the Au substrate. Under these conditions, the local pressure applied on the TMD MLs was calculated as a function of the pressing depth of the tip with a step of 0.2 nm.

SUPPLEMENTARY MATERIALS

Supplementary material for this article is available at <https://science.org/doi/10.1126/sciadv.abm5236>

REFERENCES AND NOTES

1. M. Bernardi, M. Palummo, J. C. Grossman, Extraordinary sunlight absorption and one nanometer thick photovoltaics using two-dimensional monolayer materials. *Nano Lett.* **13**, 3664–3670 (2013).
2. J. S. Ross, P. Klement, A. M. Jones, N. J. Ghimire, J. Yan, D. Mandrus, T. Taniguchi, K. Watanabe, K. Kitamura, W. Yao, D. H. Codon, X. Xu, Electrically tunable excitonic light-emitting diodes based on monolayer WSe₂ p–n junctions. *Nat. Nanotechnol.* **9**, 268–272 (2014).
3. H. Lee, I. Kim, C. Park, M. Kang, J. Choi, K.-Y. Jeong, J. Mun, Y. Kim, J. Park, M. B. Raschke, K.-D. Park, Inducing and probing localized excitons in atomically thin semiconductors via tip-enhanced cavity-spectroscopy. *Adv. Funct. Mater.* **31**, 2102893 (2021).
4. K.-D. Park, T. Jiang, G. Clark, X. Xu, M. B. Raschke, Radiative control of dark excitons at room temperature by nano-optical antenna-tip Purcell effect. *Nat. Nanotechnol.* **13**, 59–64 (2018).
5. H. Moon, G. Grosso, C. Chakraborty, C. Peng, T. Taniguchi, K. Watanabe, D. Englund, Dynamic exciton funneling by local strain control in a monolayer semiconductor. *Nano Lett.* **20**, 6791–6797 (2020).

6. M. G. Harats, J. N. Kirchhof, M. Qiao, K. Greben, K. I. Bolotin, Dynamics and efficient conversion of excitons to trions in non-uniformly strained monolayer WS_2 . *Nat. Photonics* **14**, 324–329 (2020).
7. J. Lee, S. J. Yun, C. Seo, K. Cho, T. S. Kim, G. H. An, K. Kang, H. S. Lee, J. Kim, Switchable, tunable, and directable exciton funneling in periodically wrinkled WS_2 . *Nano Lett.* **21**, 43–50 (2020).
8. M. A. Haque, M. T. A. Saif, Strain gradient effect in nanoscale thin films. *Acta Mater.* **51**, 3053–3061 (2003).
9. J. Feng, X. Qian, C.-W. Huang, J. Li, Strain-engineered artificial atom as a broad-spectrum solar energy funnel. *Nat. Photonics* **6**, 866–872 (2012).
10. A. Singh, A. K. Singh, Origin of n-type conductivity of monolayer MoS_2 . *Phys. Rev. B* **99**, 121201 (2019).
11. H. Lee, J. Y. Woo, D. Y. Park, I. Jo, J. Park, Y. Lee, Y. Koo, J. Choi, H. Kim, Y.-H. Kim, M. S. Jeong, S. Jeong, K.-D. Park, Tip-induced strain engineering of a single metal halide perovskite quantum dot. *ACS Nano* **15**, 9057–9064 (2021).
12. Y. Koo, Y. Kim, S. H. Choi, H. Lee, J. Choi, D. Y. Lee, M. Kang, H. S. Lee, K. K. Kim, G. Lee, K.-D. Park, Tip-induced nano-engineering of strain, bandgap, and exciton funneling in 2D semiconductors. *Adv. Mater.* **33**, 2008234 (2021).
13. R. Schmidt, I. Niehues, R. Schneider, M. Drueppel, T. Deilmann, M. Rohlfiing, S. M. De Vasconcellos, A. Castellanos-Gomez, R. Bratschitsch, Reversible uniaxial strain tuning in atomically thin WSe_2 . *2D Mater.* **3**, 021011 (2016).
14. K. Dolui, I. Rungger, S. Sanvito, Origin of the n-type and p-type conductivity of MoS_2 monolayers on a SiO_2 substrate. *Phys. Rev. B* **87**, 165402 (2013).
15. H. J. Conley, B. Wang, J. I. Ziegler, R. F. Haglund Jr., S. T. Pantelides, K. I. Bolotin, Bandgap engineering of strained monolayer and bilayer MoS_2 . *Nano Lett.* **13**, 3626–3630 (2013).
16. T. P. Darlington, C. Carmesin, M. Florian, E. Yanev, O. Ajayi, J. Ardelean, D. A. Rhodes, A. Ghiotto, A. Krayev, K. Watanabe, T. Taniguchi, J. W. Kysar, A. N. Pasupathy, J. C. Hone, F. Jahnke, N. J. Borys, P. J. Schuck, Imaging strain-localized excitons in nanoscale bubbles of monolayer WSe_2 at room temperature. *Nat. Nanotechnol.* **15**, 854–860 (2020).
17. M. Kulig, J. Zipfel, P. Nagler, S. Blanter, C. Schüller, T. Korn, N. Paradiso, M. M. Glazov, A. Chernikov, Exciton diffusion and halo effects in monolayer semiconductors. *Phys. Rev. Lett.* **120**, 207401 (2018).
18. S. Z. Uddin, H. Kim, M. Lorenzon, M. Yeh, D.-H. Lien, E. S. Barnard, H. Htoon, A. Weber-Bargioni, A. Javey, Neutral exciton diffusion in monolayer MoS_2 . *ACS Nano* **14**, 13433–13440 (2020).
19. S. Konabe, S. Okada, Effect of Coulomb interactions on optical properties of monolayer transition-metal dichalcogenides. *Phys. Rev. B* **90**, 155304 (2014).
20. M. Palummo, M. Bernardi, J. C. Grossman, Exciton radiative lifetimes in two-dimensional transition metal dichalcogenides. *Nano Lett.* **15**, 2794–2800 (2015).
21. X. Chen, H.-R. Park, M. Pelton, X. Piao, N. C. Lindquist, H. Im, Y. J. Kim, J. S. Ahn, K. J. Ahn, N. Park, D.-S. Kim, S.-H. Oh, Atomic layer lithography of wafer-scale nanogap arrays for extreme confinement of electromagnetic waves. *Nat. Commun.* **4**, 2361 (2013).
22. R. Zhang, V. Koutsos, R. Cheung, Elastic properties of suspended multilayer WSe_2 . *Appl. Phys. Lett.* **108**, 042104 (2016).
23. N. Lundt, E. Cherotchenko, O. Iff, X. Fan, Y. Shen, P. Bigenwald, A. Kavokin, S. Höfling, C. Schneider, The interplay between excitons and trions in a monolayer of $MoSe_2$. *Appl. Phys. Lett.* **112**, 031107 (2018).
24. M. Currie, A. T. Hanbicki, G. Kioseoglou, B. J. Jonker, Optical control of charged exciton states in tungsten disulfide. *Appl. Phys. Lett.* **106**, 201907 (2015).

Acknowledgments

Funding: This work was supported by the 2018 Research Fund (1.180091.01) of UNIST (Ulsan National Institute of Science and Technology) and the National Research Foundation of Korea (NRF) grant funded by the Korea government (MEST) (2019K2A9A1A06099937 and NRF-2020R1C1C1011301). H.-R.P. acknowledges NRF-2021R1A2C1008452. S.H.C. and K.K.K. acknowledge the support by the Institute for Basic Science (IBS-R011-D1). K.K.K. acknowledges the Basic Research Program through the National Research Foundation of Korea (NRF) funded by the Ministry of Science, ICT, and Future Planning (2018R1A2B2002302). **Author contributions:** H.L., Y.K., and K.-D.P. conceived the experiments. H.L. and Y.K. performed the TEPL spectroscopy and control experiments. S.K., H.-T.L., G.J., H.-R.P., and H.C. designed and fabricated the nanogap. S.H.C. and K.K.K. prepared and transferred TMD MLs on the Au nanogap device. J.C. performed theoretical calculation and modeling of exciton distribution. H.L., Y.K., J.C., M.K., and K.-D.P. analyzed the data, and all authors discussed the results. H.L., Y.K., and K.-D.P. wrote the manuscript with contributions from all authors. K.-D.P. supervised the project. **Competing interests:** The authors declare that they have no competing interests. **Data and materials availability:** All data needed to evaluate the conclusions in the paper are present in the paper and/or the Supplementary Materials.

Submitted 23 September 2021

Accepted 14 December 2021

Published 4 February 2022

10.1126/sciadv.abm5236

Drift-dominant exciton funneling and trion conversion in 2D semiconductors on the nanogap

Hyeongwoo LeeYeonjeong KooJinseong ChoiShailabh KumarHyoung-Taek LeeGangseon JiSoo Ho ChoiMingu KangKi Kang KimHyeong-Ryeol ParkHyuck ChooKyoung-Duck Park

Sci. Adv., 8 (5), eabm5236. • DOI: 10.1126/sciadv.abm5236

View the article online

<https://www.science.org/doi/10.1126/sciadv.abm5236>

Permissions

<https://www.science.org/help/reprints-and-permissions>

Use of think article is subject to the [Terms of service](#)